

Facile preparation of ZnO/TiO₂ nanocomposite photocatalysts and study of their photocatalytic performance

S. Lin^{*}, L. Songyuan, F. Yaochong

School of Physics and Electronics, Henan University, Kaifeng, 475000, Henan, China

Due to its strong photocatalytic activity, chemical stability, resistance to chemical and optical corrosion, and non-toxic qualities, TiO₂ has received a lot of attention as a significant semiconductor material. One of the main areas of research in the field of photocatalysis has always been the system made of ZnO, another significant semiconductor, which has stronger physical and chemical characteristics and photocatalytic activity than TiO₂ and ZnO alone. The performance of the photocatalysts can be optimized by adjusting the ratio of the components in the complexes. It was found that the catalytic activity of the particulate ZnO nano photocatalysts could be improved by trace TiO₂ addition and high TiO₂ concentration in the complex, with higher degradation efficiency for methyl orange under simulated solar illumination. The enhanced performance was attributed to the high photogenerated electron-hole separation rate caused by the increased surface oxygen vacancy defects and the enhanced interfacial charge transfer of the pluralistic heterojunction structure. In addition, there is a certain selectivity of ZnO and TiO₂ for the photocatalytic degradation of methylene blue and methyl orange, which is related to the charged nature of the catalyst surface and the ionic nature of the pollutant molecules. The inhibitor studies revealed that the degradation reactions of methylene blue and methyl orange involved the active species hydroxyl radicals, superoxide radicals, and photogenerated holes formed on the catalyst surface, with superoxide radicals dominating the methyl orange reaction. The produced photocatalysts' great stability was validated by cycling experiments. Further research on the impact of catalyst dosage and pH of the contaminant solution on the photocatalytic performance of the catalysts revealed that an increase in catalyst dosage resulted in a greater number of active sites for contaminant molecules and incident light, which increased the efficiency of contaminant degradation. In an alkaline environment, the efficiency of the catalyst for photodegradation of pollutants was significantly increased due to the high concentration of strongly oxidizing hydroxyl radicals contained in the alkaline solution.

(Received September 22, 2023; Accepted December 13, 2023)

Keywords: Photocatalysis, Multiple heterojunctions, Oxygen vacancies, ZnO, TiO₂

* Corresponding author: linshen97@163.com

<https://doi.org/10.15251/JOR.2023.196.739>

1. Introduction

The research on photocatalytic degradation of environmental contaminants utilising metal oxide semiconductors as catalysts has attracted increasing attention because environmental pollution has grown to be one of the key issues affecting human life and progress at the moment [1]. TiO_2 as an important semiconductor material, has been widely studied for its high photocatalytic activity, chemical stability, resistance to chemical and optical corrosion, and non-toxic properties. The system composed with another important semiconductor, ZnO, has better physicochemical properties and photocatalytic activity than single TiO_2 and ZnO, and has been one of the hot spots for research in the field of photocatalysis [2]. In the preparation and activity studies of photocatalytic materials, the size effect has been at the centre of attention. Nanoparticles are ideal for photocatalytic materials due to their large specific surface area [3]. But precisely because of their huge specific surface and high surface activity, they frequently experience agglomeration and deactivation during research and application, turning into a barrier in the study of semiconductor photocatalysis. The source of the rich and peculiar properties that distinguish nanostructured materials from conventional materials is the small size effect and surface effect of nano cells, on the one hand, and the coupling effect and synergistic effect produced by the ordered combination of nano building blocks, on the other hand[4]. Therefore, the use of nanoparticles as building blocks and the preparation of macroscale materials through convenient and controllable strategies for the assembly of multi-level nanostructures has the potential to be an effective way to solve the above problems.

In fact, in the composite system of ZnO and TiO_2 , the conduction band bottom potential of ZnO is more negative than that of TiO_2 , while the valence band top potential of TiO_2 is more positive than that of ZnO [5]. Compared to single oxide semiconductors, this nanocomposite has a stepped energy level structure, which promotes the separation of photogenerated electron-hole pairs, prolongs the lifetime of charge carriers and improves the light absorption capacity to a certain extent [6]. The novel ZnO/ TiO_2 clay nanostructured photocatalyst can be prepared by sol-gel method, [7] showed that the photocatalyst can effectively degrade acetaminophen and antipyrine, and the excellent performance originates from the heterojunction between TiO_2 , ZnO and layered clay, which effectively reduces the probability of electron-hole complexation and promotes the surface migration and reaction of photogenerated carriers. [8] prepared multilayer ZnO/ TiO_2 heterojunction films on a fluorine-doped tin oxide conducting substrate using a layer-by-layer self-assembly process, and the photocurrent response of the heterojunction films was five times higher than that of TiO_2 films of similar thickness due to the interfacial charge transfer effect between TiO_2 and ZnO. In addition, fan-shaped and spike-shaped ZnO/ TiO_2 nano heterojunction structures were prepared based on a hydrothermal method, where the spike-shaped ZnO/ TiO_2 nanomaterials exhibited better catalytic activity in the photocatalytic degradation of methyl orange, which was attributed to their larger specific surface area.

Compared with the above methods, we have shown superiority in the preparation of nanocomposite photocatalysts with heterojunction structures using a modified polymer network gel method [9]. The samples prepared by this method showed better crystallinity, more uniform particle distribution and larger specific surface area. Therefore, in this paper, we continued to prepare ZnO/ TiO_2 nanocomposite photocatalysts using the same modified polymer network gel method and investigated the effect of the ratio of ZnO and TiO_2 content in the composite

photocatalysts on their catalytic degradation of methylene blue and MO properties under simulated solar irradiation, as well as the effect of catalyst stability, content and pH of the contaminant solution on the catalyst activity [10].

2. Experimental section

2.1. Reagents

Zn(Ac)₂·2H₂O, NaOH, Sodium dodecyl sulfate, butyl titanate, anhydrous ethanol, triethanolamine and methyl orange were all commercially available analytically pure reagents, and the experimental water was deionized water.

2.2. Preparation of ZnO powder

2.2.1. Preparation of flower-shaped ZnO powder

Zn(Ac)₂ solution (1 mol/L) and NaOH (4 mol/L) were mixed at a zinc-base molar ratio of Zn²⁺:OH⁻ = 1:6 at room temperature and pressure, then deionized water was added to fix the volume so that the initial concentration of Zn²⁺ was 0.2 mol/L to obtain a nearly transparent solution with Zn(OH)₄²⁻ as the precursor. The reaction solution was aged in a water bath at 85°C for 5 h to give a white precipitate, which was filtered, washed and dried naturally at room temperature to give a flower-like ZnO.

2.2.2. Preparation of ZnO in rods

Zn(Ac)₂ solution (1 mol/L) and NaOH (4 mol/L) were mixed at room temperature and pressure in the molar ratio of Zn²⁺:OH⁻ = 1:6, and a certain amount of sodium dodecyl sulfate was added, followed by deionized water to fix the initial concentration of Zn²⁺ at 0.2 mol/L. After stirring for 1.5 h at room temperature, the reaction solution was aged in a water bath at 85°C for 5 h. The reaction product was filtered, washed and dried naturally at room temperature. The reaction product was filtered, washed and dried naturally at room temperature to obtain ZnO in the form of rods.

2.3. Preparation of TiO₂ powder

Take 17 mL of butyl titanate into 34 mL of anhydrous ethanol, add 4.8 mL of glacial acetic acid while stirring, stir for 30 minutes, then slowly drop in 1 mL of distilled water and 10 mL of ethanol and continue to stir for 1 hour to obtain a light yellow, uniform and transparent sol. The sol was left to stand for 2 days to obtain a TiO₂ gel. The gel was dried at 100°C for 5-6 hours to obtain a pale yellow dry gel. The dry gel is held at 500°C for 2 hours and cooled naturally to room temperature to obtain TiO₂ powder.

2.4. Preparation of ZnO/TiO₂ complexes

Following the method of [11-14], ZnO in the form of flowers or rods was taken into anhydrous ethanol, the pH was adjusted to 8.5, a certain amount of triethanolamine and a trace of deionized water was added, and the dispersion was sonicated for 30 minutes and then continued to be stirred for 5 hours. Then a mixture of different amounts of ethyl titanate and anhydrous ethanol was added, stirred for 5 hours, then extracted, washed, dried naturally and finally calcined at 500°C for 2 hours.

2.5. Photocatalytic reaction with methyl orange as a substrate

Experiments for the photocatalytic degradation of methyl orange solution were carried out in a homemade reaction apparatus. 0.0800g of ZnO/TiO₂ complex or pure ZnO and TiO₂ powder was mixed and stirred with 100.00mL of methyl orange solution with a concentration of 10.00mg/L. The reaction was dispersed well with ultrasound before light irradiation and dark adsorption reaction was carried out for 30min to ensure the adsorption-desorption equilibrium [15]. The reaction was then irradiated with a 160W high-pressure mercury lamp, and at regular intervals, a certain volume of the solution was removed and the absorbance was measured at a wavelength of 464nm using deionized water as a reference, and the degradation rate of the solution was calculated based on the absorbance. The degradation rate (η) was calculated according to the following formula.

$$\eta = \left[(A_0 - A_1) / A_0 \right] * 100\% \quad (1)$$

The chemical reagents involved in the experiments were all analytically pure, among which anhydrous glucose (C₆H₁₂O₆), the reagent used for catalyst synthesis, was purchased from Tianjin Fu Chen Chemical Reagent Co. Tartaric acid (C₄H₆O₆) was purchased from Tianjin Comio Chemical Reagent Co., Ltd. and zinc nitrate hexahydrate (Zn(NO₃)₂·6H₂O), titanium dioxide (TiO₂), acrylamide (C₃H₅NO) and N,N' methylenebisacrylamide (C₇H₁₀N₂O₂) were purchased from Chengdu Kolon Chemical Co; Methyl orange (MO) and methylene blue (MB) were purchased from Tianjin Jinbei Fine Chemical Co. and Chengdu Kolon Chemical Co, The pH adjusters glacial acetic acid (C₂H₄O₂) and ammonia (NH₃·H₂O) were purchased from Tianjin Fuyu Fine Chemical Co. and Chengdu Kolon Chemical Co. Deionized water (resistivity of 18.25 MΩ) was used for all synthesis and treatment.

2.6. Photocatalytic degradation of organic pollutants

All catalytic degradation experiments were carried out at room temperature using a Beijing Porphyry PLS-SXE300D high pressure xenon lamp to simulate a solar light source [16-19]. Here is how the experiment was conducted: 100 ml of the pollutants' 4 mg/L aqueous solution was sonicated with 0.05 g of the produced catalyst for 5 minutes. The suspension was exposed to light (irradiation intensity of 120 mW/cm²) for the photocatalytic reaction once the adsorption-desorption equilibrium between the catalyst material and the contaminant molecules was reached. The photocatalytic reaction was carried out under light (irradiation intensity of 120 mW/cm²). At regular intervals during the catalytic reaction, 6 ml of the suspension was removed and centrifuged (6,000 rpm for 5 min) and placed in a V-1100D visible spectrophotometer (Shanghai Me pro Delta Instruments Co., Ltd.) to determine the absorbance of the reacted pollutant solution. Finally, the degradation rate of the contaminants was calculated

$$\nu = \frac{A_0 - A}{A_0} \times 100\% = \frac{C_0 - C}{C_0} \times 100\% \quad (2)$$

where ν is the degradation rate, A_0 and A are the absorbance of the pollutant solution before and after illumination respectively, C_0 and C are the corresponding pollutant concentrations.

In the inhibitor experiments, the reactive species were first removed from the sample surface using the inhibitors benzoquinone, isopropanol, and disodium EDTA. Next, the sample was sonicated into an aqueous solution of the pollutant and the inhibitor, which was then allowed to stand to achieve adsorption-desorption equilibrium before being subjected to photocatalytic degradation [20–23]. In addition, the initial pH of the contaminant solution was adjusted using glacial acetic acid and ammonia, and the catalytic reaction conditions were further optimised by adjusting the catalyst dosage. The irradiation intensity of the light source was 200 mW/cm² in the catalytic experiments as well as in the cycling experiments.

3. Results and analysis

3.1. Analysis of photocatalytic properties

Figure 1 demonstrates the photocatalytic degradation efficiency of commercial TiO₂, prepared pure ZnO and ZnO/TiO₂ nanocomposite catalysts with different TiO₂ contents for MB and MO under simulated solar illumination. All samples were able to completely degrade MB and MO, with the photocatalytic degradation rates reaching over 93% for MB when exposed to 80 min of light and over 90% for MO when exposed to 90 min of light [24–26]. To better illustrate the catalytic degradation efficiency of the catalyst samples, the corresponding kinetic curves were fitted (see Table 1 for the fitted parameters) and the results are shown in the inset of Figure 1 (a) and (b), where the slope of the curve reflects the rate of organic pollutant degradation. In the inset of Figure 1(a), the rate of MB degradation for each catalyst sample was ranked from highest to lowest as TiO₂>ZT0.5>ZT0.25>ZT0.002>ZT0.02>ZT0.1>ZnO; In the inset of Figure 1(b), the rate of MO degradation for each catalyst sample is ranked from highest to lowest ZT0.002>ZT0.5>ZnO>ZT0.02>TiO₂>ZT0.25>ZT0.1. It can be seen that the commercial TiO₂ samples under simulated sunlight irradiation are more suitable for the catalytic degradation of MB, while the prepared ZnO samples are more suitable for the catalytic degradation of MO. For the nanocomposite catalysts, the photocatalytic degradation efficiency of the catalysts for MB decreases significantly as the TiO₂ content decreases. However, for the degradation of MO, trace amounts of TiO₂ (ZT0.002) further optimized the photocatalytic activity of the ZnO nano catalyst, with the catalyst activity decreasing and then increasing as the TiO₂ content continued to increase. Table 2 compares the photocatalytic degradation efficiencies of various semiconductor composite photocatalysts for organic pollutants that have recently been reported in the literature, and the results demonstrate that the ZnO/TiO₂ composite catalyst developed in this work has a superior efficiency [27]. All catalyst samples' physical phase, microstructure and morphology, surface chemical state, defect state, and optoelectronic capabilities were meticulously characterised in order to more clearly illustrate the physical nature behind these occurrences.

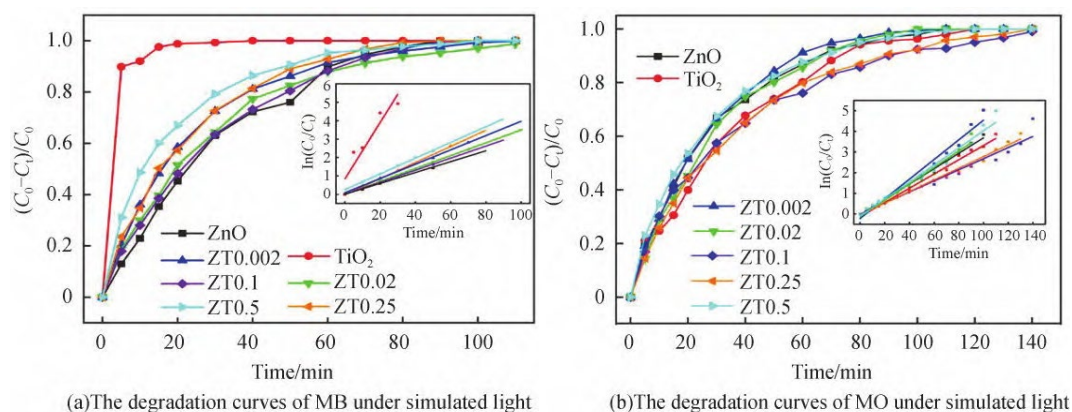


Fig. 1. Degradation rate curves of MB and MO under simulated solar illumination for pure ZnO, commercial TiO₂ and ZnO/TiO₂ nanocomposite catalysts (inset shows the corresponding quasi-level kinetic fit curves).

Table 1. Performance parameters of pure ZnO, commercial TiO₂ and ZnO/TiO₂ nanocomposites for the degradation of MB and MO under simulated solar light.

| Sample | Organic pollutant | Linear fitting equation | Apparent chemical reaction rate constant | Linearly dependent coefficient R |
|------------------|-------------------|-------------------------|------------------------------------------|----------------------------------|
| ZnO | MB | $y=0.02948x+0.0091$ | 0.02948 | 0.99398 |
| | MO | $y=0.03739x-0.05044$ | 0.03739 | 0.99697 |
| TiO ₂ | MB | $y=0.15303x+0.84102$ | 0.15303 | 0.94234 |
| | MO | $y=0.03455x-0.13914$ | 0.03455 | 0.99150 |
| ZT0.002 | MB | $y=0.03884x+0.08503$ | 0.03884 | 0.99922 |
| | MO | $y=0.04774x-0.22842$ | 0.04774 | 0.98853 |
| ZT0.02 | MB | $y=0.03494x+0.00414$ | 0.03494 | 0.99992 |
| | MO | $y=0.03996x-0.1466$ | 0.03996 | 0.98757 |
| ZT0.1 | MB | $y=0.03268x+0.00891$ | 0.03268 | 0.99972 |
| | MO | $y=0.02699x-0.02011$ | 0.02699 | 0.98010 |
| ZT0.25 | MB | $y=0.04379x-0.02402$ | 0.04379 | 0.99945 |
| | MO | $y=0.02930x-0.04849$ | 0.02930 | 0.99473 |
| ZT0.5 | MB | $y=0.04265x+0.25968$ | 0.04265 | 0.99897 |
| | MO | $y=0.04142x-0.11219$ | 0.04142 | 0.98695 |

Table 2. Degradation of organic pollutants by different semiconductor composite photocatalysts.

| Type of catalysts | Organic pollutant | Initial concentration | Catalyst dose | Light irradiated | Irradiation time | Removal efficiency | References |
|--------------------------------------------------|-------------------|-----------------------|---------------|-------------------------------------|------------------|--------------------|------------|
| ZnO/TiO ₂ | MB | 4mg/L | 0.5g/L | Simulated sunlight | 80min | 93% | This work |
| | MO | | | | 90 min | 90% | |
| ZnO/TiO ₂ | MB | 5 mg/L | 1.5g/L | UV, λ_{\max} =365nm | 60 min | 100% | [3] |
| | MO | 20 mg/L | 50 g/L | | 90 min | 99% | |
| CuO/ZnO | MO | 10mmol/L | -- | Visible light | 5h | 90% | [5] |
| ZnO/TiO ₂ | MB | 0.01mmol/L | -- | Simulated sunlight | 180 min | 100% | [12] |
| CnO/TiO ₂ | MB | 5 mg/L | -- | Simulated sunlight | 60 min | 40% | [13] |
| NiO/TiO ₂ | MO | 10 mg/L | 1.43 g/L | UV, λ_{\max} =253.8nm | 1h | 87.4% | [14] |
| | | | | Visible light | | 95.7% | |
| TiO ₂ /Fe ₂ O ₃ | MB | 0.01mmol/L | 1 g/L | UV | 5h | 95.3% | [22] |
| | | | | Visible light | 2h | 96% | |
| CdS/ TiO ₂ | MO | 5 mg/L | 2 g/L | Simulated sunlight | 120 min | 95.4% | [23] |
| ZnO/Cds | MB | 0.01mmol/L | 0.25 g/L | Sunlight | 120 min | 100% | [24] |

3.2. Physical phase analysis

Figure 2 shows the XRD patterns of commercial TiO₂, pure ZnO and ZnO/TiO₂ nanocomposite catalysts. The diffraction peaks marked # in the pattern correspond to the (100), (002), (101), (102), (110), (103), (112) crystal faces of hexagonal fibrous stone phase ZnO (JCPDS No. 36-1451) and the diffraction peaks marked * correspond to the (101), (200) crystal faces of anatase phase TiO₂ (JCPDS No. 21- 1272). As the TiO₂ content increases, the diffraction peaks belonging to TiO₂ in the ZnO/TiO₂ nanocomposite catalyst samples gradually increase, while the diffraction peaks belonging to ZnO gradually weaken. When the TiO₂ addition was increased to 10 mol/mol, zinc titanate (Zn₂TiO₄) in the cubic phase appeared in the composite catalyst samples and increased with the TiO₂ content, as seen in the diffraction peaks of labelled * in the plots (JCPDS No.25-1164). The presence of Zn₂TiO₄ and the increase in composition may explain the lower actual molar ratios in the composite catalyst samples compared to the experimental ratios. In addition, the average grain size of all samples was calculated using Scherrer's formula (equation (3)) based on the XRD measurements, as shown in Table 3.

$$D(hkl) = \frac{k\lambda}{\beta \cos \theta} \quad (3)$$

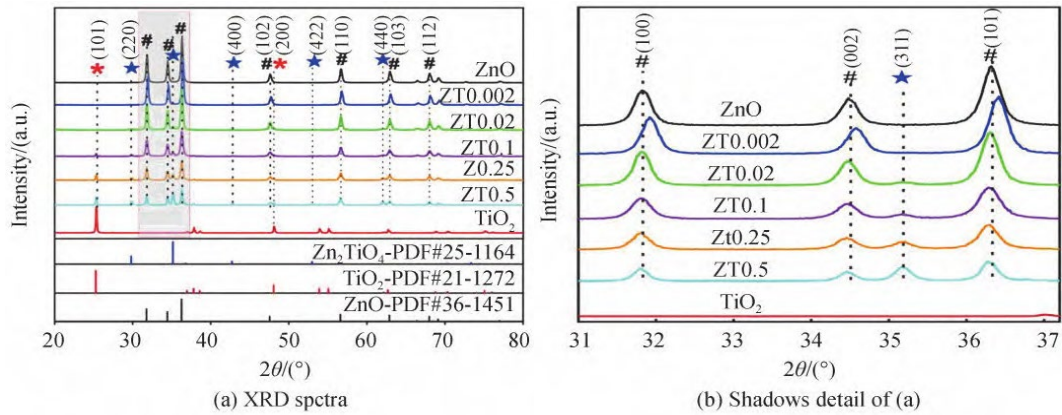


Fig. 2. XRD patterns of pure ZnO, commercial TiO₂ and ZnO/TiO₂ nanocomposite catalysts.

Where $D(hkl)$ is the grain diameter along the direction perpendicular to the grain plane (hkl) , $k = 0.89$, λ is the wavelength of the X ray, taken as 0.154 06 nm, β is the full width of the diffraction peak half-peak (in radians) and θ is the Bragg diffraction angle (position of the diffraction peak, in radians).

According to Table 3, the average grain size of all catalyst samples with a large proportion of TiO₂ composite did not change significantly compared to pure ZnO. This is because the presence of TiO₂ and Zn₂/TiO₄ in composite form does not affect the growth of ZnO nanocrystals.

Table 3. Parameters of pure ZnO, commercial TiO₂ and ZnO/TiO₂ nanocomposites.

| Samples | Number | Average grain size / nm | Specific surface area / (m ² g ⁻¹) |
|------------------|--------|-------------------------|-----------------------------------------------------------|
| ZnO | 26 | 63.85 | 9.1333 |
| TiO ₂ | 38 | 116.79 | 9.7673 |
| ZT0.002 | 25 | 79.42 | 7.2763 |
| ZT0.02 | 26 | 60.40 | 9.2541 |
| ZT0.1 | 25 | 46.54 | 8.9524 |
| ZT0.25 | 27 | 36.37 | 9.4703 |
| ZT0.5 | 29 | 69.26 | 6.7426 |

3.3. Microstructural and morphological analysis

Figures 3 (a), (b), (d) and (e) show the high resolution transmission electron microscopy

images of samples ZT0.002 and ZT0.5 respectively. As shown in Figure 3 (a) and (b), the observed lattice stripe spacing is 0.260 nm and 0.283 nm respectively, attributed to the (002) and (100) crystal planes of the hexagonal fibrous ZnO phase.

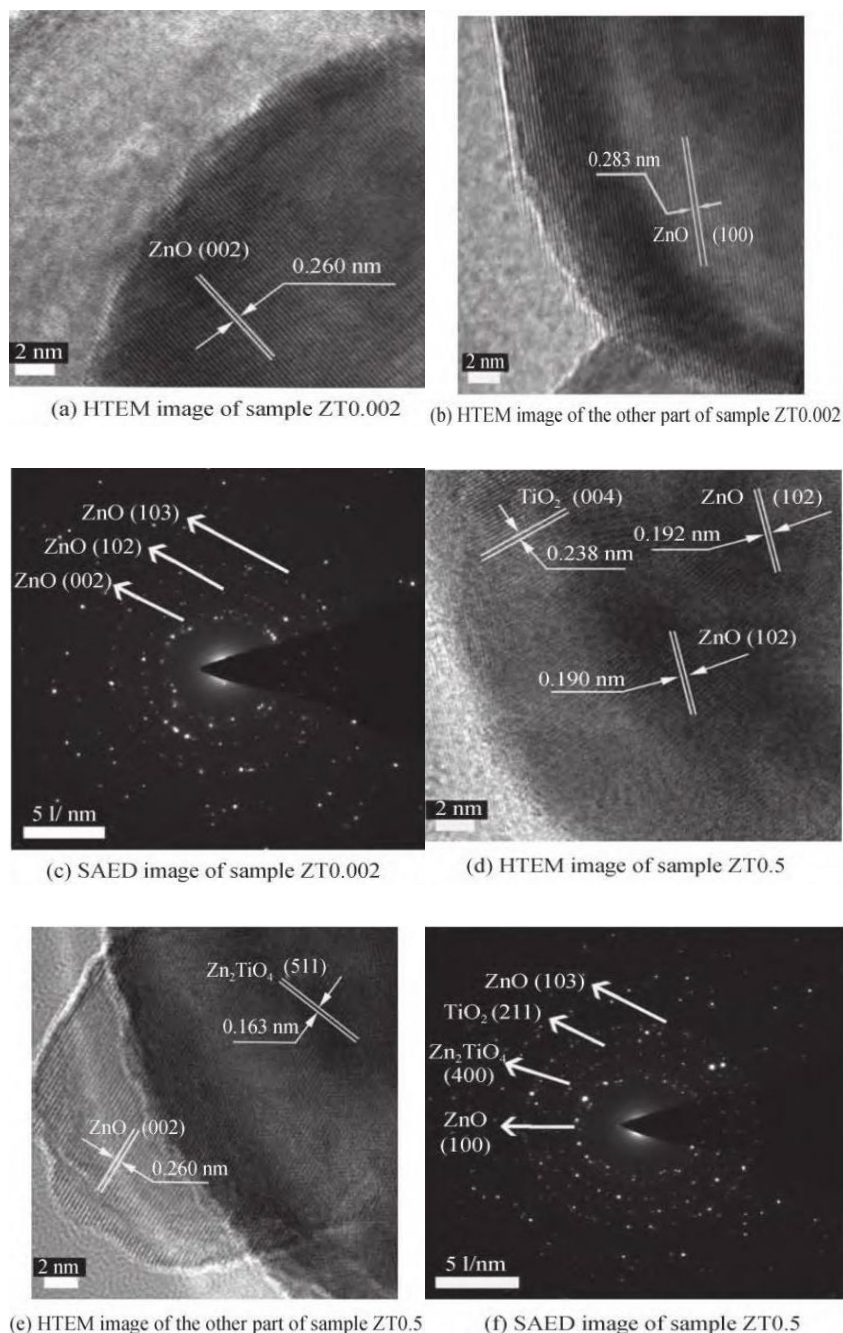


Fig. 3. TEM images and SAED images of samples ZT0.002 and ZT0.5.

In Figure 3(d) and (e), a variety of different lattice stripes are observed with distances between stripes of 0.163 nm, 0.190 nm (or 0.192 nm) and 0.260 nm and 0.238 nm, corresponding to the (511) crystal plane of cubic phase Zn_2TiO_4 , the (102) and (002) crystal planes of hexagonal

fibrillated zincite phase ZnO, the (004) crystal plane of anatase phase (004) crystal plane spacing of TiO₂. This indicates that the composite bulk TiO₂ sample ZT0.5 contains not only the ZnO phase, but also the TiO₂ phase as well as the newly formed Zn₂TiO₄ phase. Further observations show that a multifaceted nano heterojunction structure is formed between ZnO, TiO₂ and Zn₂TiO₄. This heterostructure leads to the formation of a stepped energy level structure through interfacial effects, which hinders the photogenerated charge complex and prolongs its lifetime, thus enhancing the photocatalytic activity of the samples. The Selected Area Electron Diffraction (SAED) patterns of samples ZT0.002 and ZT0.5 are shown in Figure 3(c) and (f). The SAED patterns were calibrated using the CrysTBox (v1.10) software and the results further confirm that there is no other phase composition in sample ZT0.002 and that the trace amount of TiO₂ composite does not change the structure of the catalyst material. In contrast, a large amount of TiO₂ complexation led to the formation of a multifaceted nano heterojunction structure of the catalyst material.

The morphology and particle size of nanoparticulate catalysts usually affect their catalytic performance. Figure 4 shows the surface morphology of all catalyst samples, and the statistically obtained particle size distribution is given by Figure 5 [28]. The commercial TiO₂ samples had better crystallinity than the other samples, although all samples were composed of sphere-like polygonal nanoparticles with a wide particle size variability. Additionally, the composite catalyst had more small and medium-sized particles and had more severe particle agglomeration as the TiO₂ level rose. However, the number of big particles rose and particle agglomeration decreased when the TiO₂ adding level reached 50 mol/mol. The average particle size calculated from the statistical distribution of particle size is shown in Table 3, The average particle sizes of the ZnO, TiO₂, ZT0.002, ZT0.02, ZT0.1, ZT0.25 and ZT0.5 samples were 63.84, 116.78, 79.41, 60.39, 46.53, 36.36 and 69.25 nm respectively. For nanoparticulate catalysts, the smaller the particle size and the less agglomeration of particles, the larger the specific surface area of the catalyst. Therefore, based on the adsorption data of the catalyst samples on N₂ in the relative pressure range of 0.05 to 0.3, the specific surface area was determined using the multi-point BET method, as shown in Table 3, and the specific surface areas of the ZnO, TiO₂, ZT0.002, ZT0.25 and ZT0.5 samples were 9.133 2, 9.767 2, 7.276 2, 9.470 2, and It is clear that the specific surface area of the ZT0.002 and ZT0.5 samples with better catalytic performance is smaller compared to the other samples, which indicates that the change in specific surface area due to particle and particle agglomeration does not have a significant effect on the catalytic performance of the catalysts.

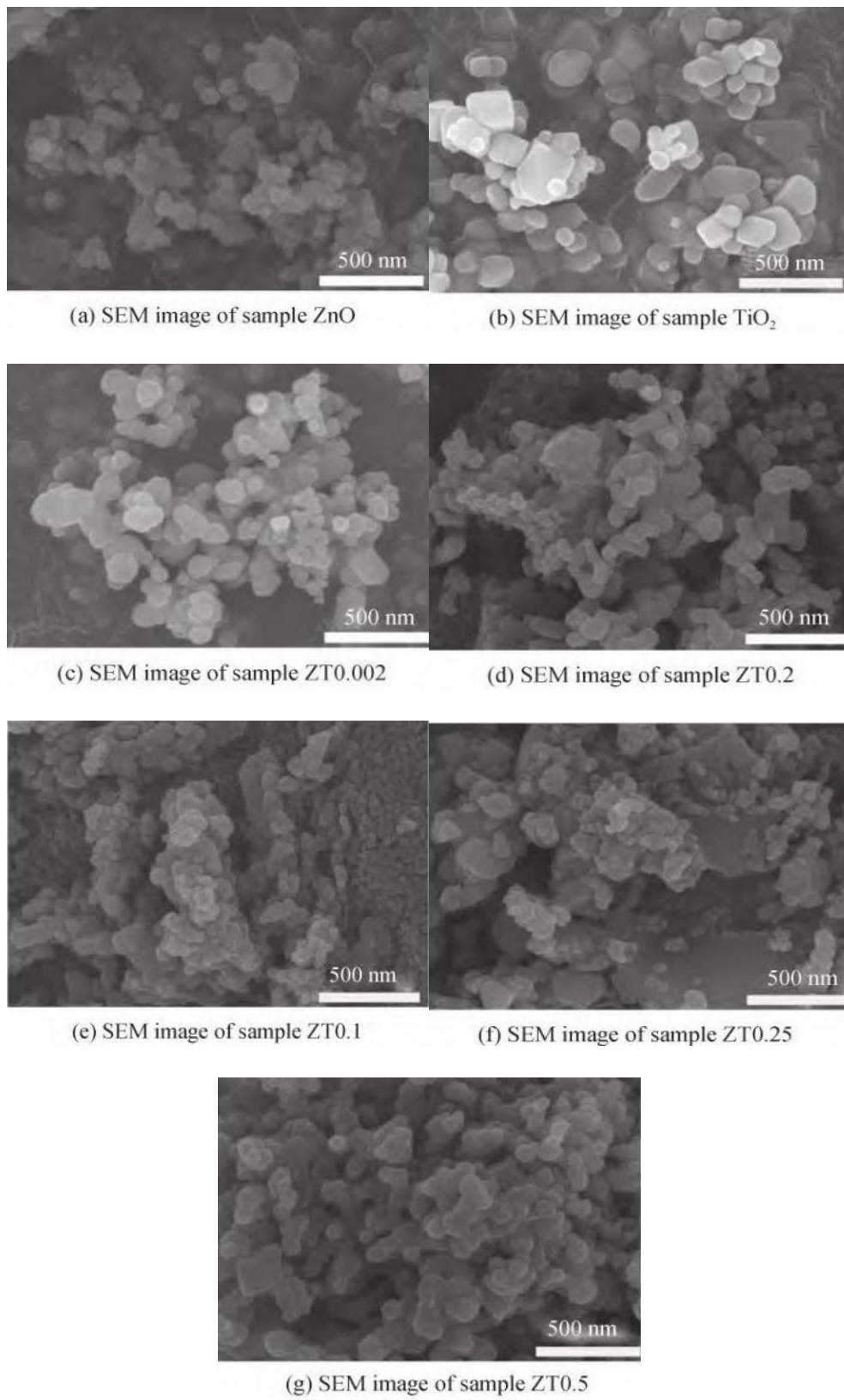


Fig. 4. SEM image of the sample.

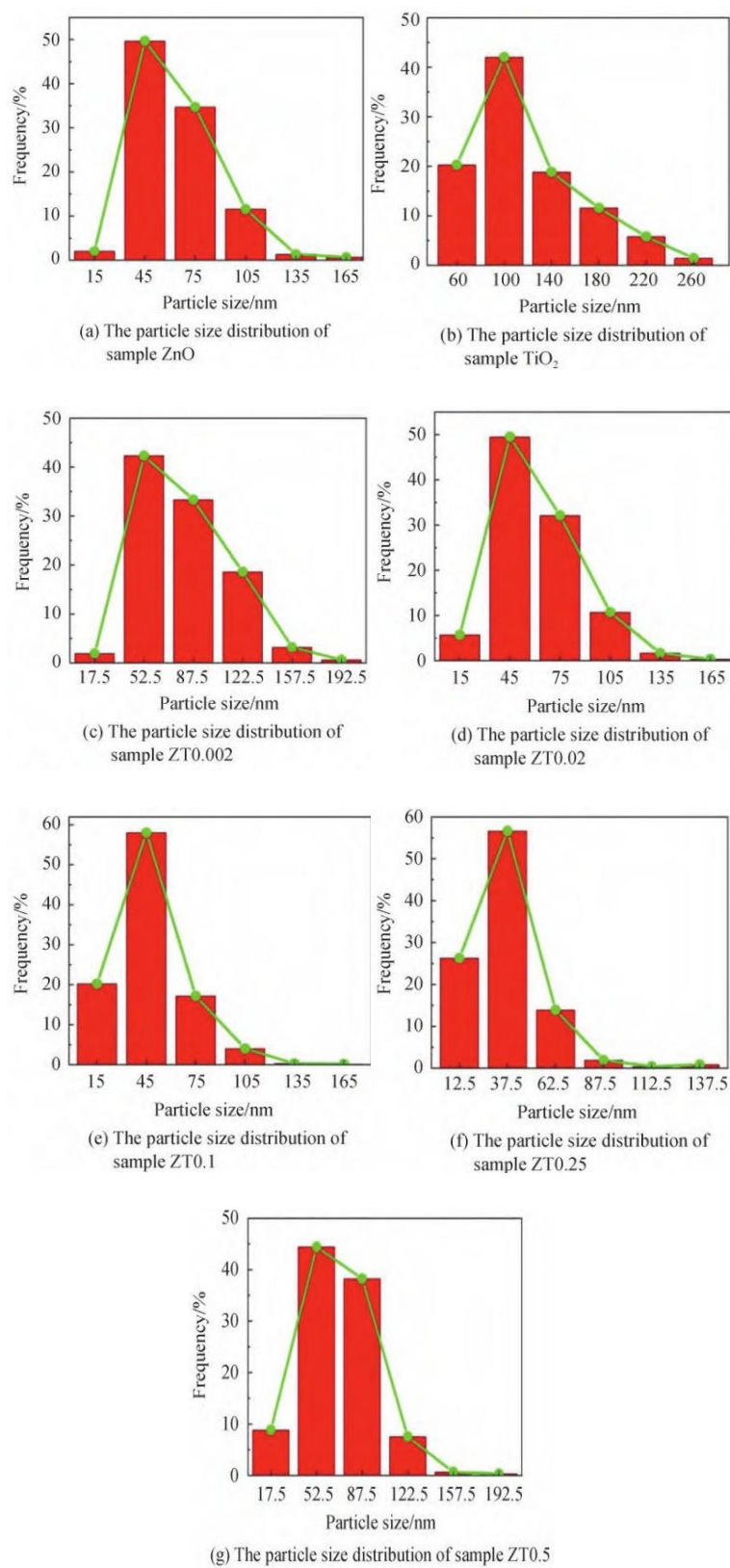


Fig. 5. Particle size distribution of samples.

3.4. Surface chemical state analysis

Further research was done on the surface chemical states, defect states, and photoelectric characteristics of pure ZnO and ZnO/TiO₂ nanocomposite catalysts. The XPS full spectrum revealed signal peaks linked to the components Zn, Ti, and O, as illustrated in Figure 6(a). These findings demonstrate the great purity of the produced catalyst samples and suggest that the element C discovered in the samples may have come from the XPS instrument itself as well as minute amounts of organic debris that persisted in the samples after calcination.

The high-resolution Zn 2p XPS spectra (Figure 6(b)) show that the peaks located at binding energies of 1021.4 eV and 1044.5 eV correspond to Zn 2p_{3/2} and Zn 2p_{1/2}, respectively, indicating the presence of Zn in the samples as Zn²⁺ ions [29]. The high-resolution Ti 2p XPS spectrum (Figure 6(c)) shows that the peaks located at binding energies of 458.8 eV and 464.4 eV correspond to Ti 2p_{3/2} and Ti 2p_{1/2}, respectively, with a separation of approximately 5.6 eV between the two peaks, demonstrating the presence of Ti₄₊ ions in the sample [30]. In addition, signals relating to Ti 2p were detected in samples ZT0.02, ZT0.25 and ZT0.5, but not in sample ZT0.002, which is consistent with the XRD results. The high resolution O 1s XPS spectrum (Figure 6(d)) shows that the spectrum exhibits an asymmetric XPS peak with the presence of a shoulder peak, which was split into two peaks using a Gaussian fit at 530.3 ± 0.1 eV and 531.7 ± 0.1 eV respectively, consistent with the lattice Oxygen (OL) and Chemical Adsorption Oxygen (OC) in the catalyst samples. Adsorption Oxygen (OC) species in the catalyst samples [31]. In actuality, water molecules can readily adsorb on the surface of oxide nanomaterials and split apart to generate hydroxyl groups due to the abundance of oxygen vacancy defects on their surface [30].

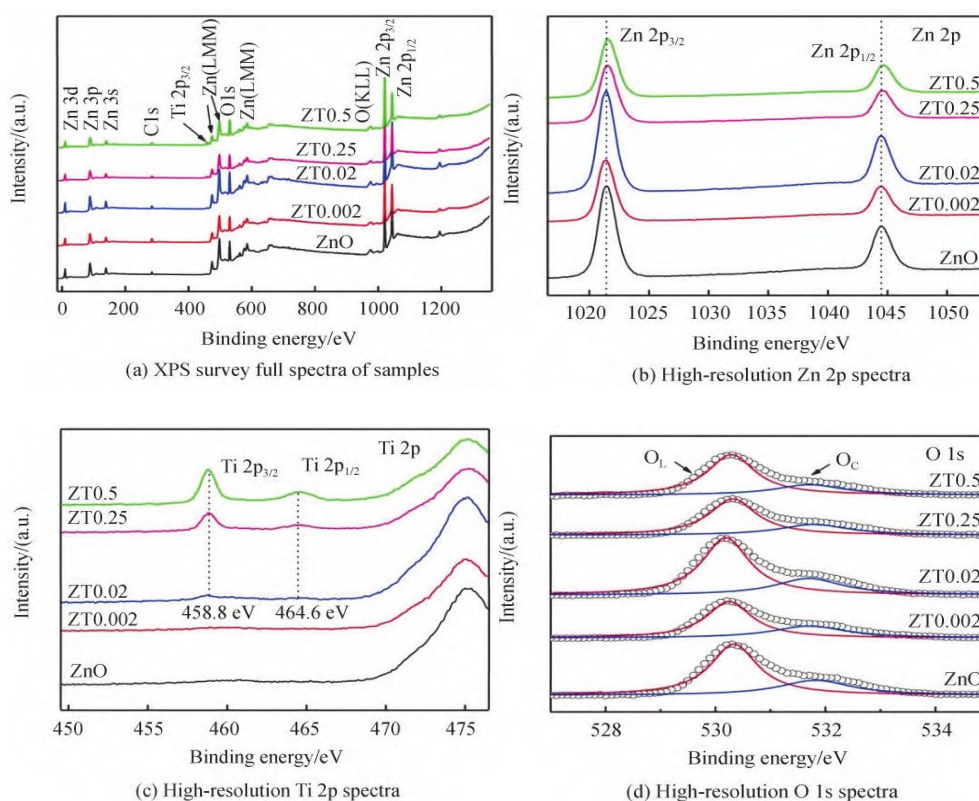


Fig. 6. XPS pattern of the sample.

Thus, the number of surface oxygen vacancies correlates with the intensity of the OC counterpart peaks in the O 1s XPS spectra. These oxygen vacancy defects can operate as electron traps to prevent the complexation of photogenerated electron-hole pairs[26]. The XPS spectra of the O 1s were quantified by calculations comparing the percentages of the two oxygen species, as shown in Figure 7. Compared to pure ZnO, the OC content of the composite sample with trace TiO₂ (ZT0.002) was significantly higher, increasing from 31% to 34%, indicating that the introduction of trace TiO₂ during the synthesis process contributed to the increased number of oxygen vacancy defects on the catalyst surface. When the introduced TiO₂ content was increased to 2 mol/mol (ZT0.02), the surface oxygen vacancy defects were instead reduced. At the same time, the surface oxygen vacancy defects of the samples are further reduced when large amounts of TiO₂ are introduced, and gradually decrease with increasing content. The reduced surface oxygen vacancy defects result from the secondary crystallization of ZnO and TiO₂ nanocrystals during the synthesis process as well as the improved crystal quality due to the increased content of the more crystalline TiO₂.

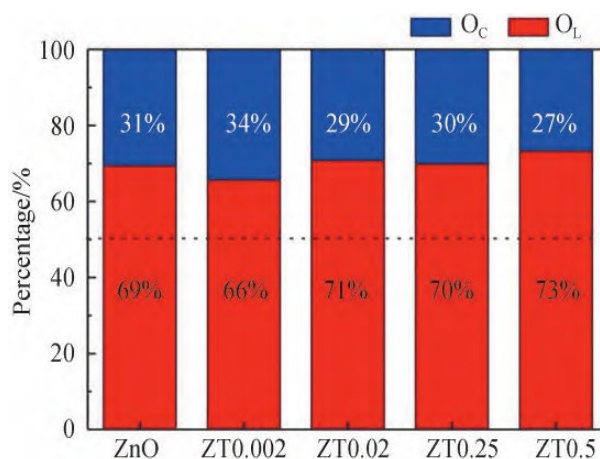


Fig. 7. Proportional oxygen content of samples.

3.5. Defective state analysis

Figure 8 illustrates the room temperature electron paramagnetic resonance (EPR) spectra of the catalyst samples. All samples exhibit a strong EPR signal peak at $g=2.0045$, which is caused by the trapping of unpaired electrons by oxygen vacancy defects formed in the catalyst material, and therefore the intensity of this peak can reflect the concentration of oxygen vacancy defects in the material. As the TiO₂ content increases, the EPR signal peak of the ZnO/TiO₂ nanocomposite catalyst gradually becomes weaker, i.e. the concentration of oxygen vacancy defects gradually decreases, which is consistent with the XPS findings regarding surface oxygen vacancy defects. However, for pure ZnO samples, a high EPR signal peak implies a high concentration of oxygen vacancy defects, which is contrary to the findings of XPS. The reason for this is that EPR reflects the total oxygen vacancy defects in the material, including both in vivo and surface oxygen vacancy defects, whereas XPS mainly reflects surface oxygen vacancy defects. Combining the results of XPS and EPR, it can be seen that the synthesized ZnO samples are richer in oxygen vacancy defects in vivo and have poorer crystal quality. As the amount of TiO₂

compound increases, the internal oxygen vacancy defects decrease and the crystal quality improves, and the concentration of surface oxygen vacancy defects first increases and then decreases. In general, surface oxygen vacancies act as electron traps that can promote surface chemistry and reduce the complexation of photogenerated electron-hole pairs while oxygen vacancies in living things act as electron traps that can't do either. Therefore, a high defect ratio between internal and surface oxygen vacancies is advantageous for the catalyst's high photocatalytic performance.

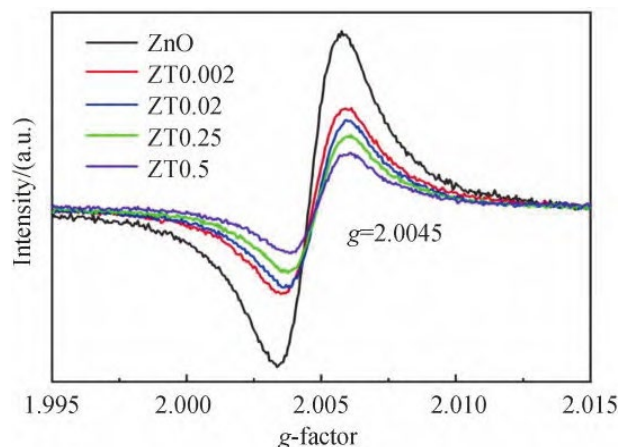


Fig. 8. Electron paramagnetic resonance spectrum of the sample at room temperature.

3.6. Photoelectric characterization

Figure 9 shows the UV-Vis absorption spectra of all samples. As can be seen in Figure 9, commercial TiO_2 exhibits the weakest light absorption, where the low UV absorption may be due to the large particles, as the smaller the nanoparticle size, the stronger the UV absorption; the low visible absorption is due to the high crystal mass, when the intra band jump caused by the oxygen vacancy defect energy level is significantly reduced. For the ZnO/TiO_2 nanocomposite catalyst samples, UV and visible light absorption is enhanced and the absorption band edges are significantly red-shifted. It was further observed that, with the exception of the ZT0.1 sample, the light absorbance and the wavelengths corresponding to the absorption band edges of the other composite catalyst samples were in between those of the commercial TiO_2 and ZnO samples, and these phenomena were directly related to the particle size and oxygen vacancy concentration of the catalyst particles. The analysis shows that the commercial TiO_2 sample has the largest nanoparticle size, the best crystal quality and correspondingly the least oxygen vacancy defects. However, the synthesized ZnO samples have smaller nanoparticle sizes, poorer crystal quality and more oxygen vacancies. In actuality, as oxygen vacancies rise, the oxide semiconductor material's band gaps become faulty, increasing the absorption of visible light. The localised defect energy levels near to the valence band become continuous when this vacancy defect rises to a particular level, which causes the valence band top to shift higher and the band gap width to shorten [23]. As a result, the synthetic ZnO exhibits higher visible light absorption and absorption band edges closer to longer wavelengths. The band gaps of the commercial TiO_2 and synthetic ZnO samples, calculated by the plot equation (equation (4)), are 3.12 and 3.17 eV respectively, as shown in the inset in Figure 9.

$$(ahv)^{1/n} = A(hv - E_g) \quad (4)$$

where a is the absorbance index, $h\nu$ is the photon energy, A is a constant and E_g is the band gap width of the semiconductor. Because absorbance or α has no effect on E_g , a in Equation. can be replaced by absorbance; the index n is related to the type of semiconductor, usually ZnO is a direct bandgap semiconductor and n is taken as 1/2, while TiO₂ is an indirect bandgap semiconductor and n is taken as 2.

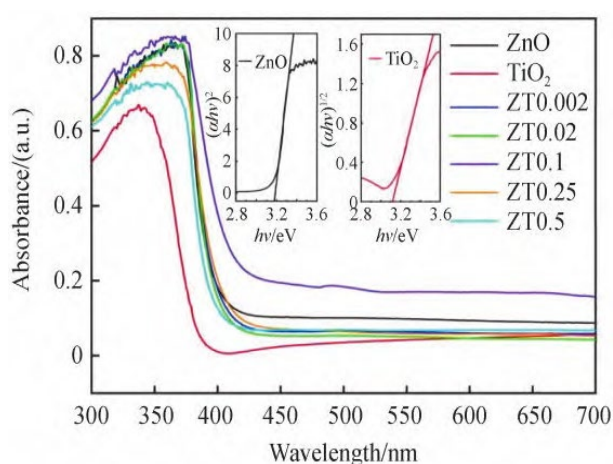


Fig. 9. UV-Vis absorption spectrum of the sample.

For photocatalysts, high light absorption indicates higher quantum yields, implying that more electron-hole pairs are produced by photoexcitation, but it is often the number of electrons and holes that migrate to the catalyst surface to participate in the redox reaction that determines catalytic efficiency, which is directly related to the electron-hole separation rate in the catalyst. Surface photovoltage (SPV) spectroscopic measurements are indicative of the efficiency of photogenerated charge carrier separation in materials. Figure 10 shows the SPV spectra of all catalyst samples, and the inset shows an enlargement of the SPV spectra of ZnO and ZT0.1 in the 320-400 nm optical band. The signal peaks located in the UV region originate from the voltages generated on the conductive surface of Indium Tin Oxide (ITO) and aluminium pole plates after the effective separation of electron-hole pairs generated by the intrinsic band-band jumps of the samples under UV excitation. The SPV peaks of commercial TiO₂ were located at 351 nm, while the SPV peaks of ZnO and ZnO/TiO₂ composite photocatalysts were located at 372±4 nm, and the composite samples all showed a voltage response to blue light near 400 nm, which was consistent with the results of UV-Vis absorption spectroscopy. The intensity of the SPV peaks increased and then decreased with increasing TiO₂ content, reaching a maximum at ZT0.002, except for the ZT0.1 sample, where the intensity of the SPV peaks was higher than that of ZnO. These results were related to the microstructural changes of the catalysts, when a trace amount of TiO₂ (e.g.

ZT0.002 and ZT0.02) was added during the synthesis of ZnO catalysts, the trace amount of TiO₂ regulated the nucleation, crystallization and crystal growth processes of ZnO, with less oxygen atom deletion within the crystal and increased crystal mass, while more oxygen atom deletion on the crystal surface formed more surface oxygen vacancy defects. The heterojunction formed between ZnO, TiO₂ and Zn₂, TiO₄ promotes the separation of photogenerated carriers when a large amount of TiO₂ (e.g. ZT0.25 and ZT0.5) is compounded, thus the SPV response of the compound catalysts is greater than that of ZnO. The higher SPV response of TiO₂ than ZnO was attributed to the higher crystal mass and less particle agglomeration, which reduced the complexation of photogenerated carriers inside the crystal and at the grain boundaries.

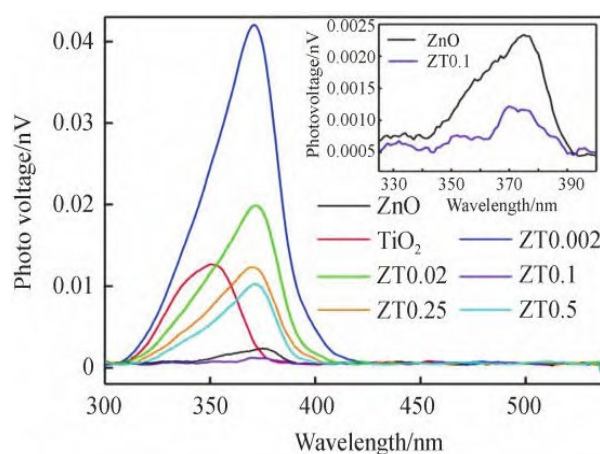


Fig. 10. Surface photo-voltage profile of the sample.

4. Photocatalytic mechanism

In order to elucidate the reasons for the changes in the performance of the composite catalysts and the catalytic reaction mechanism, inhibitor experiments were carried out to identify the active species involved in the degradation reactions of organic pollutants. When p-benzoquinone (a superoxide radical trapping agent) was added to the aqueous MB solution, the degradation efficiency of the ZT0.002 catalyst samples under simulated solar illumination was somewhat reduced as shown in Figure 11 (a) and (b), however, degradation was completely inhibited when p-benzoquinone was added to the aqueous MO solution as shown in Figure 11 (c) and (d). When isopropyl alcohol (a hydroxyl radicals ($\cdot\text{OH}$) inhibitor) and disodium EDTA (a vacancy scavenger) were added to the aqueous MB and MO solutions respectively, the degradation efficiency of both was reduced to a greater extent. In summary, in the photocatalytic reaction system containing ZT0.002 catalyst samples, the surface active species involved in the degradation of MB and MO included $\cdot\text{OH}$, $\cdot\text{O}_2^-$ and cavities, with $\cdot\text{O}_2^-$ playing a dominant role in the degradation reaction of MO.

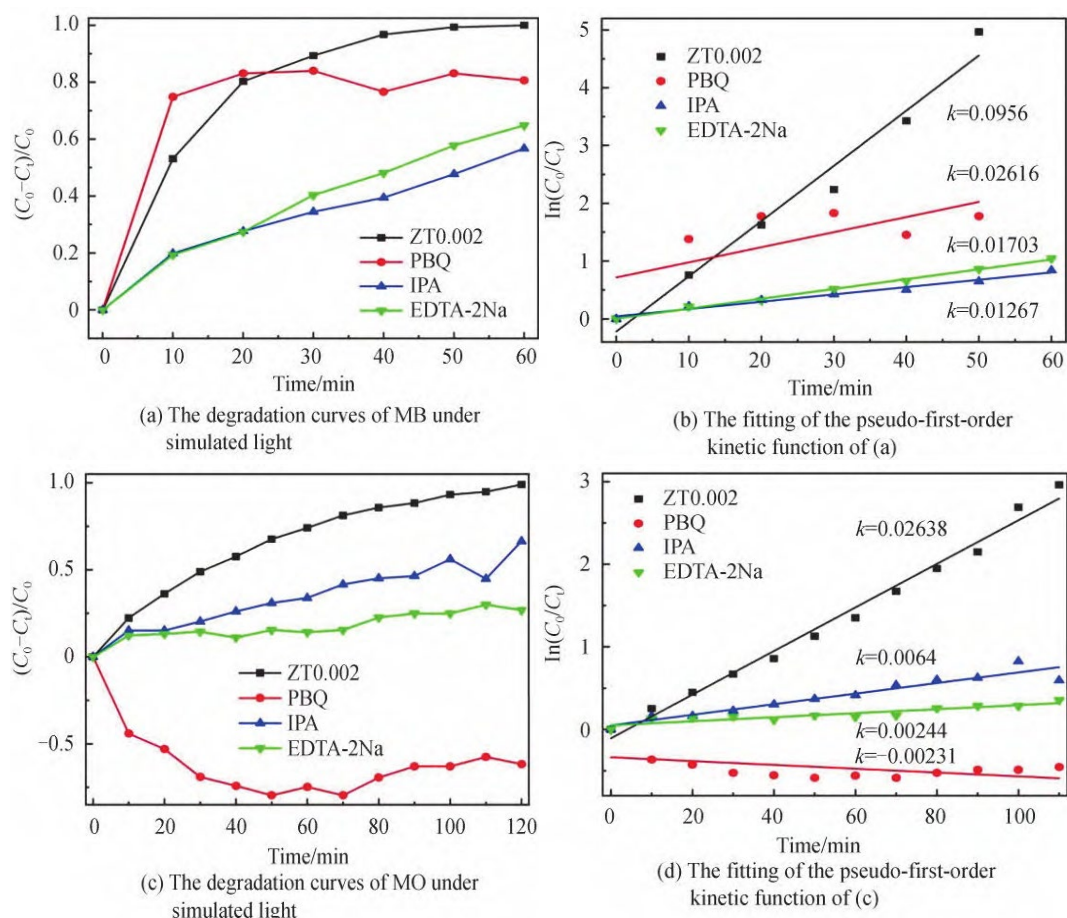


Fig. 11. Effect of different inhibitors on the photodegradation of MB and MO by ZT0.002 nanocomposite catalyst under simulated solar illumination.

Figure 12 depicts the catalytic mechanism of the ZnO/TiO₂ nanocomposite photocatalyst under simulated solar irradiation and is used to illustrate the mechanism by which the catalyst microstructure affects the photocatalytic activity. When trace amounts of TiO₂ were compounded with ZnO (e.g. ZT0.002 sample), no other components were found to be present in the composite catalyst, so the enhanced photocatalytic activity mainly originated from the increase in surface oxygen vacancy defects, and the enhancement mechanism is shown in Figure 12(a). With simulated solar irradiation, the vast majority of photogenerated charge carriers in the ZT0.002 catalyst are generated by UV-induced band-band leap at photon energies ($h\nu$) greater than the ZnO band gap energy (3.17 eV), i.e. electrons in the valence band absorb the energy of the photons and leap to the conduction band, thereby creating holes in the valence band, while some visible light can excite the oxygen vacancy defect energy level (usually as a shallow sender energy level near the valence band, see Figure 12(a)) and the conduction band, increasing the number of photogenerated charge carriers. In addition, surface oxygen vacancy defects act as active sites that not only inhibit the complexation of photogenerated electron-hole pairs by trapping electrons, but also increase the adsorption of pollutant molecules [24,26]. These positive changes promote the formation of $\cdot\text{OH}$ and $\cdot\text{O}_2^-$, see reaction equations (5) and (6), accelerating the decomposition of pollutant molecules. Therefore, the ZnO/TiO₂ nanocomposite photocatalysts compounded with

trace amounts of TiO_2 are more active in the degradation of MO compared to pure ZnO and commercial TiO_2 .



When a large amount of TiO_2 is compounded with ZnO (e.g. ZT0.5 sample), the enhanced MO photocatalytic degradation efficiency mainly arises from the multiplicative heterogeneous interfacial charge transfer effect, as shown in Figure 12(b). Based on the previous work, the energy level positions of ZnO, TiO_2 , Zn_2TiO_4 are plotted in the figure. Since the band gap energies of these three are 3.17, 3.12 and 3.00 eV respectively, and the conduction band potentials of Zn_2TiO_4 are more negative than those of ZnO, TiO_2 , which in turn are more negative than those of TiO_2 , their valence band potentials change in the same trend, thus forming a staggered type II heterojunction structure between ZnO, TiO_2 , Zn_2TiO_4 . When light with photon energy greater than the band gap energy of the three catalysts is irradiated onto the surface of the composite catalyst, the excited electrons will migrate from the Zn_2TiO_4 conduction band to the ZnO conduction band and then to the TiO_2 conduction band, while the photogenerated holes will migrate from the TiO_2 valence band to the ZnO valence band and then to the Zn_2TiO_4 valence band in turn. As the migration of the photogenerated charge carriers occurs, an internal electric field is formed at the interface between Zn_2TiO_4 and ZnO, and between ZnO and TiO_2 , which effectively promotes the directional separation of the photogenerated electrons-hole, extending the lifetime of the charge carriers and increasing the photocatalytic activity.

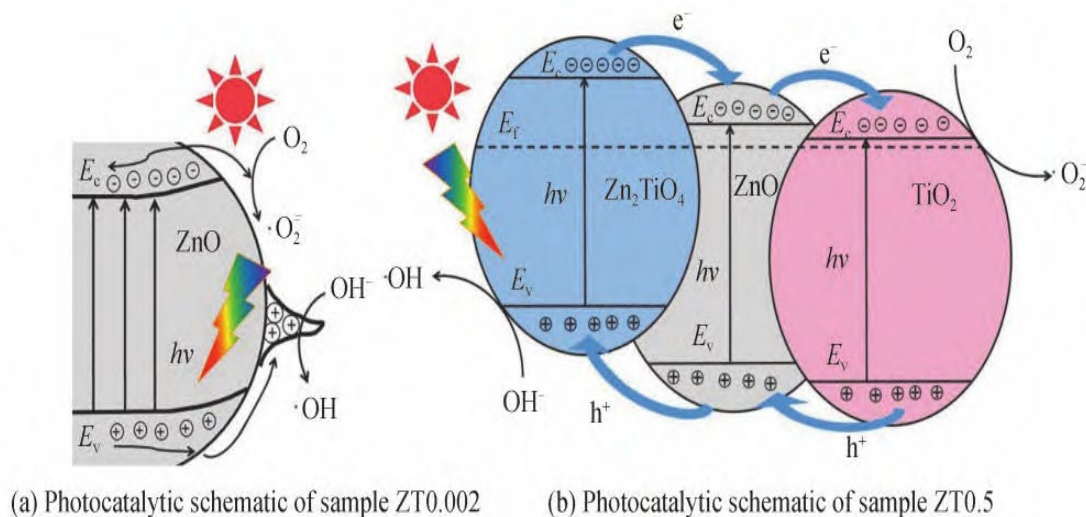


Fig. 12. Photocatalytic mechanism.

The reason for the photocatalytic degradation of MO and MB by ZnO and TiO_2 , respectively, may be related to the pH of the pollutant solution [25]. The pH of the solution determines the charged nature of the catalyst surface and thus affects the adsorption of dye molecules on its surface. Due to the amphoteric behavior of most metal oxides, the following two equilibrium reactions were considered.



At a pH higher than the zero charge potential of the catalyst, the catalyst surface is negatively charged according to the above equilibrium relationship, and MB, being a cationic dye, is more readily adsorbed by the negatively charged TiO₂ sample surface compared to the anionic dye MO. This accelerated the photodegradation of MB by TiO₂ and the rate of photodegradation of MB was much greater than its rate of photodegradation of MO. In their study of the photocatalytic properties of TiO₂ polyvinyl alcohol (PVA) complexes, JASEELA P K et al. found that they were highly selective for the cationic dye MB due to electrostatic adsorption between themselves and MB and a negative surface ξ potential, whereas the anionic dye MO was difficult to adsorb on the TiO₂-PVA surface.

5. Exploring the application of catalysts

To explore the practical applications of the catalysts, the stability and catalyst dosage as well as the effect of pH of the pollutant solution on the catalytic activity were investigated. As shown in Figure 13 (a) and (d), the photocatalytic efficiency of the ZT0.002 catalyst samples did not change significantly after five cycles of photodegradation of MB and MO respectively under simulated sunlight irradiation, indicating that the photocatalytic stability of the prepared samples was good. Figure 13(b) and (e) show the degradation curves of ZT0.002 with different catalyst doses (0.01-0.3 g/L) for MB and MO under simulated solar irradiation, respectively. It can be seen that the increase in catalyst dose increases the efficiency of pollutant decomposition for both MB and MO. The increased efficiency can be attributed to the fact that more catalysts provide more active sites for pollutant molecules and incident light, increasing the redox reaction on the catalyst surface. Figure 13(c) and (f) shows the degradation curves of MB and MO by ZT0.002 catalyst samples under simulated sunlight irradiation for different initial pH (3-11) pollutant solutions, respectively. The ZT0.002 catalyst samples were significantly more efficient in photocatalytic degradation of pollutants in alkaline (pH>7) environment, while their photocatalytic degradation efficiency decreased in acidic (pH<7) environment, especially the degradation of MO was extremely slow. When the pH is less than 7, according to the reaction equations (6) and (7), the catalyst surface exhibits a positive charge, which is not conducive to the surface adsorption of the cationic dye MB. At the same time, when the solution is at a high pH, it contains a high concentration of OH⁻ ions, which can further generate hydroxyl radicals with strong oxidizing properties (\cdot OH). During the catalytic reaction, hydroxyl radicals dominate the photocatalytic behavior of the anionic dye MO in solution, so the rate of photocatalytic degradation of MO is enhanced in alkaline environments.

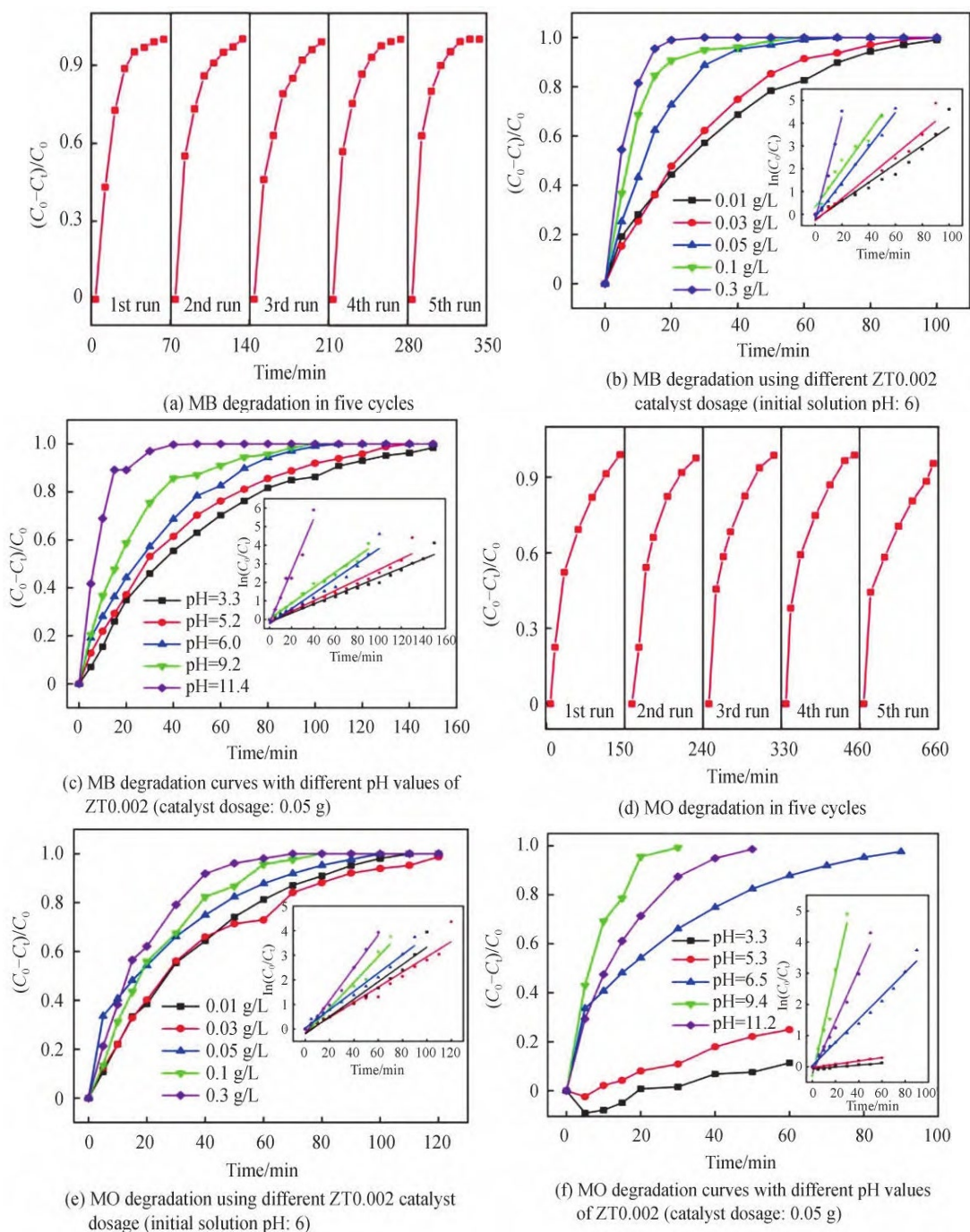


Fig. 13. Efficiency curves for the degradation of MB and MO of ZT0.002 samples under simulated light under different external conditions (inset is a quasi-level kinetic fit).

6. Conclusion

This study used the adsorbed water layer on the ZnO surface as a reactor to create ZnO/TiO₂ composite photocatalysts with micro and nanostructures. When calcined at 500 degrees Celsius, the nano-sized TiO₂ was consistently bonded to the micrometer-sized rod- or flower-like ZnO surface, and the complexes were composed of hexagonal-phase ZnO and anatase TiO₂. The

hydrolysis of the adsorbed water layer has the potential to alter the compositions of the complexes. By adjusting the amount of Ti (OC₄H₉)₄ added during the hydrolysis process, it is possible to modify the composition of the complexes. It was discovered through preliminary research on the photocatalytic performance of ZnO/TiO₂ complexes with various ratios that the best photocatalytic effect was obtained when the ratio of flower-type ZnO/TiO₂ catalysts was 1:3, and the best photocatalytic effect was obtained when the composite ratio of rod-shaped ZnO/TiO₂ composite catalysts was 1:1. The investigation of reaction kinetics revealed that the catalytic reactions of both composite rod and floral catalysts were first-order. The outcomes of the experiment also demonstrated that this micro/nanomaterial is readily recyclable while in use and may be reused. As a result, this composite photocatalyst has potential applications by partially increasing the material's photocatalytic activity through the micro/nanostructural coupling of high-quality semiconductors on the one hand, and by combining the advantages of conventional micromaterials with the small-size effect of nanoparticles on the other.

Acknowledgements

The authors would like to show sincere thanks to those techniques who have contributed to this research.

References

- [1] Hardiansyah, A. , Budiman, W. , Yudasari, N. , Isnaeni, Kida, T. , Wibowo, A. (2021), ACS omega, 6(47), 32166-32177; <https://doi.org/10.1021/acsomega.1c04966>
- [2] Zhang, B., Ren, X. , Zhao, Y. , Zhou, X. , & Hu, X. (2022), Water, Air, & Soil Pollution, 233(12), 1-12; <https://doi.org/10.1007/s11270-022-06001-0>
- [3] Ali, Q., Hussain, S., Hussain, T., Faryad, M., Ali, S., & Rizwan, M., et al. (2021), Current Analytical Chemistry, 17(1), 82-97; <https://doi.org/10.2174/15734110MTA4gMDY2x>
- [4] Li, Y., Liu, M., Zhang, M., Liu, Y., Zhao, Q., & Li, X., et al. (2023), Nano, 18(02); <https://doi.org/10.1142/S1793292023500091>
- [5] Rajendran, R., Vignesh, S., Sasireka, A., Sundar, J. K., Vairamuthu, R.. (2021), Materials Technology(12), 1-14; <https://doi.org/10.1080/10667857.2021.1968232>
- [6] Han, J. (2022), Polymers, 14(16); <https://doi.org/10.3390/polym14163230>
- [7] Nasief, O. A., Abd, A. N.. (2021), IOP Conference Series: Earth and Environmental Science, 779(1), 012057 (10pp); <https://doi.org/10.1088/1755-1315/779/1/012057>
- [8] Carolina, D. A. G., Palharim, P. H., Ramos, B., Teixeira, A. C. S. C.. (2022), Environmental Science and Pollution Research(28), 29; <https://doi.org/10.1007/s11356-021-16718-w>
- [9] Sonia, Kumari, H., Suman, Chahal, S., Devi, S., Kumar, S., et al. (2023), Applied Physics A, 129(2); <https://doi.org/10.1007/s00339-022-06288-0>
- [10] Manuel Gambín, Gabriel Pérez-Lucas, Simón Navarro. (2021), Bulletin of Environmental Contamination and Toxicology, 106(6); <https://doi.org/10.1007/s00128-021-03158-y>
- [11] Huang, J., Liang, R., Huang, Y., Li, F., & Li, T.. (2021), Journal of the Iranian Chemical

- Society, 18(3), 567-571; <https://doi.org/10.1007/s13738-020-02060-4>
- [12] Zhang, Y., Ping, X., Hao, L., He, Y., Lu, Y.. (2021), Journal of Environmental Chemical Engineering, 9(4), 105565; <https://doi.org/10.1016/j.jece.2021.105565>
- [13] Ren, Z., Li, X., Guo, L., Wu, J., & Ma, J.. (2021), Materials Letters, 292, 129635; <https://doi.org/10.1016/j.matlet.2021.129635>
- [14] Al-Musawi, T. J., Mengelizadeh, N., Sathishkumar, K., Mohebi, S., Balarak, D.. (2021), Colloids and Interface Science Communications, 45(3), 100532; <https://doi.org/10.1016/j.colcom.2021.100532>
- [15] Formica, M., Rogova, T., Shi, H., Sahara, N., Ferko, B., Farley, A. J. M., et al. (2023), Nature Chemistry, 15(5), 714-721; <https://doi.org/10.1038/s41557-023-01165-6>
- [16] Assimeddine, M., Farid, Z., Abdennouri, M., Barka, N., Lemdek, E. M., Sadiq, M.. (2023), Environmental Science and Pollution Research, 30(22), 62494-62507; <https://doi.org/10.1007/s11356-023-26417-3>
- [17] Fan, M. Z., Sun, B. Z., Jiang, J. Y., Pan, J. Y., Hu, P. H. (2023), Rare Metals, 42(6), 1912-1922; <https://doi.org/10.1007/s12598-022-02241-5>
- [18] Hou, Z., Zou, X., Pu, X., Wang, L., Geng, Y.. (2021), Journal of Solid State Chemistry, 296, 121965; <https://doi.org/10.1016/j.jssc.2021.121965>
- [19] Hajipour, P., Bahrami, A., Mehr, M. Y., Driel, W., Zhang, K.. (2021), Materials, 14(4), 763; <https://doi.org/10.3390/ma14040763>
- [20] Kouhail, M., Zakia, E. A., Abbes, B.. (2020), Current Nanomaterials, 5(3), 252-268; <https://doi.org/10.2174/2405461505999201014085242>
- [21] Thakur, O. P., Prakash, C., & Agrawal, D. K. (2002), Journal of Ceramic Processing Research, 3(2), 75-79.
- [22] Shin, D. G., Riu, D. H., Kim, H. E. (2008), Journal of Ceramic Processing Research, 9(2), 209-214.
- [23] He, K., Chen, Y., Mei, M.. (2020), Nanotechnology Reviews, 9(1), 1160-1169; <https://doi.org/10.1515/ntrev-2020-0074>
- [24] Ton, N. Q. T., Le, T. N. T., Kim, S., Dao, V. A., Vu, T. H. T.. (2020), Journal of Nanoscience and Nanotechnology, 20(4), 2214-2222; <https://doi.org/10.1166/jnn.2020.17306>
- [25] Lee, H. S. (2012), Journal of Ceramic Processing Research, 13(S2), 300-303.
- [26] Kim, I. J. (2010), Journal of Ceramic Processing Research, 11(4), 411-418.
- [27] Farahmandjou, M., Golabiyani, N. (2015), Journal of Ceramic Processing Research, 16(2), 1-4.
- [28] Wu, P., Xu, Y., Huang, Z., Zhang, J. (2015), Journal of Ceramic Processing Research, 16(1), 102-106.
- [29] Lim, C. S., Ryu, J. H., Kim, D. H., Cho, S. Y., Oh, W. C. (2010), Journal of Ceramic Processing Research, 11(6), 736-741.
- [30] Pookmanee, P., Phanichphant, S. (2009), TiJournal of Ceramic Processing Research, 10(2), 167-170.
- [31] Reyes-López, S. Y., Acuña, R. S., López-Juárez, R., Rodríguez, J. S. (2013), Journal of Ceramic Processing Research, 14(5), 627-631.